Title Page

Authors

Jordan R. Mertes[1,2], Jason D. Gulley[3], Douglas I Benn[4], Sarah S. Thompson[5],

Lindsey I. Nicholson[5]

Title

Using Structure from Motion to create Glacier DEMs and Orthoimagery from

Historical Terrestrial and Oblique Aerial Imagery

Affiliations

[1]Department of Geological and Mining Engineering and Sciences, Michigan

Technological University, Houghton, MI

[2]Department of Arctic Geology, University Centre in Svalbard, Postboks 156,

Longyearbyen, N-9170, Svalbard, Norway

[3]School of Geosciences, University of South Florida, 4202 E. Fowler Avenue, NES

107, Tampa, FL 33620-5550 USA

[4]School of Geography and Geosciences, University of St. Andrews, North Street, St.

Andrews, Fife KY16 8ST, UK

[5]Institute of Atmospheric and Cryospheric Sciences, Universität Innsbruck, 6020

Innsbruck, Austria

Abstract

Increased resolution and availability of remote sensing products, and advancements in small-scale aerial drone systems, allows observations of glacial changes at unprecedented levels of detail. Software developments, such as Structure from Motion (SfM), now allow users an easy and efficient method to generate 3D models and orthoimages from aerial or terrestrial datasets. While these advancements show promise for current and future glacier monitoring, many regions still suffer a lack of observations from earlier time periods. We report on the use of SfM to extract spatial information from various historic imagery sources. We focus on three geographic regions, the European Alps, High-Arctic Norway and the Nepal Himalaya. We used terrestrial field photos from 1896, high oblique aerial photos from 1936 and aerial handheld photos from 1978 to generate DEMs and orthophotos of the Rhone glacier, Brøggerhalvøya and the lower Khumbu glacier, respectively. Our analysis shows that applying SfM to historic imagery can generate high quality models using only ground control points. Limited camera/orientation information was largely reproduced using self-calibrated model data. Using these data, we calculated mean ground sampling distances across each site which demonstrates the high potential resolution of resulting models. Vertical errors for our models are ±5.4 m, ±5.2 m and ±3.3 m. Differencing shows similar patterns of thinning at lower Rhone (European Alps) and Brøggerhalvøya (Norway) glaciers, which have mean thinning rates of 0.31 m a^{-1} (1896-2010) to 0.86 m a^{-1} (1936-2010) respectively. On these clean ice glaciers thinning is highest in the terminus region and decreasing upglacier. In contrast to these glaciers, uneven topography, exposed ice-cliffs and debris cover on the Khumbu glacier create a highly variable spatial distribution of thinning. The mean thinning rate for the Khumbu study area was found to be 0.54±0.9 m a^{-1} (1978-2015).

Introduction

Observations from an increasing number of glacier monitoring programs have quantified the sensitivity of glaciers to regional and global climate changes that have occurred over the last several decades (Silverio and Jaquet, 2005, Paul et al., 2007, Bolch et al., 2011, Kamp et al., 2011, Diolaiuti et al., 2012, Braithwaite et al., 2013). Many locations, however, lack any glacier monitoring programs or have only short periods of data. Understanding magnitudes of changes in modern glacier mass balance would be improved if these changes could be placed in historical context. Such improvements could aid in improved forecasting of future glacial conditions and associated implications for water resources (Immerzeel et al., 2010, Thorsteinsson et al., 2013, Unger-Shayesteh et al., 2013, Soruco et al., 2015) and potential geo-hazards (Bolch et al., 2011, López-Moreno et al., 2014) by gaining more insight into past changes.

Current technology allows scientists to monitor glaciers at spatio-temporal scales that were unthinkable 20 years ago. Just over 10 years ago, a DEM for an entire glacier, at a 10 m resolution, was considered "high resolution" (Gruen and Murai, 2002). It is now possible to get stereo satellite images of glaciated regions that that can yield products, such as digital elevation models (DEMs) and orthorectified imagery, at resolutions of < 0.5 m (e.g. GeoEye, Worldview, Pleiades). Light detection and ranging (LiDAR) is a widely used technology in cryospheric sciences, both terrestrially and aerially, and has the capability of producing models of centimeter resolution and accuracy (Bhardwaj et al., 2016a). Recent advances in unmanned aerial vehicles (UAVs) and computer vision software such as Structure from Motion (SfM) and Multi-View Stereo (MVS) now allow researchers to extract 3D information from their own remotely-sensed data at high spatial and temporal

resolution (Bhardwaj et al., 2016b). While current high-resolution satellite data, aerial and terrestrial LiDAR scans and UAV surveys can help monitor present and future glacial changes in unprecedented detail, historical oblique images remain a largely untapped resource of glacier mass balance data.

Numerous studies have used older satellite and aerial photos for studying glacier changes through means of monoplotting (Kääb and Funk, 1999, Haeberli et al., 2001, Wiesmann et al., 2012), orthoplotting/orthorectification (Surazakov et al., 2007, Bhambri et al., 2011, Wang et al., 2016), or by producing actual DEMs from the imagery itself (Kääb, 2000, Baltsavias et al., 2001, Keutterling and Thomas, 2006, Bolch et al., 2011, Gabbud et al., 2016). However, many earlier aerial surveys took imagery at highly oblique angles which were primarily used for cartographic purposes (e.g. Bjork et al., 2012). Yet, using SfM, it has now become possible to extract DEMs from these older imagery sources with little to no a priori camera information, generally an important requirement for traditional photogrammetric processing.

Using SfM+MVS to extract geometric information from imagery works by matching features (e.g. pixels, pixel groups, edges) of the same subject across images that were taken from different perspectives. Following sparse 3D point cloud generation (i.e. SfM), estimation of internal orientation (IO) (e.g. focal length, radial distortion) and external orientation (EO) (i.e. X, Y, Z, roll, pitch, yaw), MVS algorithms generate a dense point cloud by extracting depth information from all pixels matched in multiple images (Agarwal et al., 2011). As a result, SfM+MVS (hereafter referred to as SfM) allows generation of 3D models of objects without having any a priori IO or EO information. Real-world coordinate systems can be assigned to models with the aid of current orthoimagery and DEMs by matching arbitrary points in the model with

their corresponding real world position. This information is then used during sparse point cloud optimization, during which the accuracy of the camera model, and the estimated camera positions and parameters can be improved through a bundle adjustment and self-calibration of the camera model (Agisoft, 2014, James and Robson, 2014, James et al., 2017). The result of such a process is that one can create a DEM and orthoimage using easily acquired imagery and identifiable ground control data.

In this study we present the results of using the SfM technique to extract geometric information and create DEMs from freely available, archival glacial imagery. Creating these historical DEMs allows us to document changes in glacier surfaces as far back as the late 19th century. We focus on three distinct geographic regions and glacial types, the European Alps clean ice glacier, high Arctic Norway clean ice glaciers and the Nepal Himalayas heavily debris-covered glacier, from 1896, 1936 and 1978 respectively. These specific cases involve different image types and compare resultant models and glacial changes on a variety of glaciers. In addition, we demonstrate how this process can be performed without detailed information about the IO and EO of the imagery, and how with precise enough GCPs, the estimated EO information becomes close to the true values.

Study Sites

Our study sites cover a range of glaciated environments from alpine to arctic and Himalayan. Within these regions, we selected glaciers that have historical images and that have also been the focus of previous glaciological investigations.

Rhone glacier, Switzerland

The Rhone glacier (46°36'N, 8°23'E) is located in the central Swiss Alps (Figure 1, A) and is the source of the Rhone river, which flows through Lake Geneva and south to the Mediterranean Sea. The glacier has some of the longest time series of observations of any glacier in the world, with length measurements dating back to 1609 and mass balance measurements dating back to 1884 (Wallinga and Wal, 1998). We selected this site because repeat terrestrial photographic surveys began during the late 19th century (Mercanton et al., 1916). In addition, the glacier's rapid retreat from the lower valley to its current position is well documented in post cards, photographs and scientific articles. The abundance of photographic, cartographic and glaciological data on the Rhone glacier have made this glacier the focus of numerous glacier-climate modelling studies, as there is plenty data available to verify model results (Roderik and Van De Wal, 1998, Sugiyama et al., 2007, Jouvet et al., 2009). For this study, we focus on the 1.1 km^2 area in the lower valley from where the glacier terminated in 1896, up to the lip of the upper hanging valley (Figure 1, A Yellow Box).

Ny Ålesund, Svalbard

The Svalbard Archipelago is located north of mainland Norway at ~76-80°N and ~10-30°E (Figure 1, B). Nearly 60% of the total area of Svalbard is glaciated (Hagen et al., 2003). We selected Brøggerhalvøya (~190 km^2), which is located around the research village of Ny Ålesund, on the northwestern coast of Spitsbergen (78°56′ N, 11°53′ E) (Figure1, B Yellow Box), as our study area because previous attempts at extracting surface information have been performed over this region. Nuth et al. (2007) interpolated DEMs from topographic maps with 50 m contour intervals, the

maps were originally derived in part from the imagery used in this study. The area

has a central mountain ridge running in a NW-SE direction with ~25 small cirque

glaciers, some of which have been the focus of numerous scientific studies (e.g. Jon

Ove and Olav, 1990, Fleming et al., 1997, Lefauconnier et al., 1999, Kohler et al.,

2007, Nuth et al., 2007, Barrand et al., 2010).

Khumbu Glacier, Nepal

The Khumbu glacier is located in the similarly named Khumbu region of the

Mahālangūr Himāl, northeast Nepal (Figure 1, C) (Carter, 1985). The glacier

accumulation zones are located in the upper reaches of mountain peaks, including

Chumbu to the west, Pumori to the north and Lhotse, Nupste and Mt. Everest to the

north and east. From the south face of Mt. Everest, the glacier flows a distance of 16

km to the terminus. Our area of interest is the lower 10 km of the glacier, located just

down glacier from the confluence of the two main tributaries, ~5000 m a.s.l. (Figure

1, C Yellow Box). The area has been chosen based on the type of imagery (i.e.

handheld cameras) and the importance of understanding the long-term evolution of

debris-covered glacier surfaces and patterns of downwasting. The glacier terminus is

at an elevation of 4900 m a.s.l. (Nakawo et al., 1999). The flow direction of this

section of the glacier runs in a NE-SW direction at 207° and the lowest 4 km of the

snout are now stagnant (Quincey et al., 2009).

Methods

   Imagery

We obtained 3 images of the Rhone glacier (Figure 2) from the Swiss Federal

Institute of Technology (ETH) Library "e-pics" imagery archive (ETH-Bibliothek,

2016). The images are terrestrial photographs taken 30 August, 1896. They are located in the collection of imagery taken by the Glaziologische Kommission der SANW. None of the images were attributed to any specific photographer, but they have similar compositions as repeat photographs of the Rhone glacier taken by Paul-Louis Mercanton during the late 19th century through to the early 20th century and were taken on the same 9x12 cm film plates (Mercanton et al., 1916). The series contained numerous photographs, but only 4 captured the lower glacier tongue. Of these four, view angles only allowed us to use three images for model recreation. We were unable to find any information pertaining to camera type, IO or EO.

We obtained 25 images of the Ny Ålesund field site (Figure 2) from the Toposvalbard database (http://toposvalbard.npolar.no), which is managed by the Norwegian Polar Institute. Images on Toposvalbard can be browsed in a GIS environment, in which each image is placed in its approximate geographic position with a marker arrow indicating the line of sight. These aerial high-oblique images were taken from roughly 3-3500 m a.s.l. during the summer of 1936 using a Zeiss 18 x 18 cm aerial camera with a focal length of 210mm (Debenham, 1938). The images were taken in a roughly south to southwest direction from above Kongsfjord, on the northern shore of the peninsula. Detailed IO and EO data have not been determined for these images.

We obtained 42 images of the Nepal field site (Figure 2) from the Japan Agency for Marine-Earth Science and Technology's Cryosphere Data Archive Partnership (CrDAP) Observational Research Database. These images are part of the 11 December 1978 aerial photo reconnaissance, which was conducted by the Japanese Glaciological Expedition in Nepal (GEN) to support large-scale glacial observations throughout the Nepal Himalaya. The photos were taken with handheld 35 mm film based cameras from a chartered low flying Pilatus Turbo Porter airplane, at angles

from high oblique to near nadir (Yabuki, 2012). Data pertaining to detailed IO and EO of the cameras used to capture these images is also unknown.

Image corrections

We adjusted contrast and exposure of all images in Adobe Photoshop Lightroom™ 6.6.1. This process was subjective and performed manually on the different sets of images to improve clarity in the areas of interest.

We made no additional adjustments to the Switzerland imagery as they appear to be slightly different dimensions (3520x2537, 3462x2635 & 3425x2632 pixels) and have no borders or fiducial markings to align.

Images from the Svalbard survey were first corrected for alignment issues caused during digitizing. We noted alignment issues when we observed that images were not exactly the same dimensions. All images were opened in a common photo editing suite, placed into individual layers and one by one were rotated and scaled slightly to align the fiducial marks around the image borders. Once this was complete, all images were cropped down to the nearest square dimension of 6370x6370 pixels.

The images from the Nepal survey were digitized to the same dimensions therefore no post resizing, alignment or cropping was performed. Images have dimensions of 2137x1535 pixels. Image watermarks pose no issue as these areas can be masked out during processing.

Reference DEMs and Orthoimages

We relied on recent high-resolution DEMs and orthoimages to identify stable ground control points (GCPs), such as boulders or mountain peaks, for georeferencing the

final models. The addition of GCPs also helps to improve the calculation of the IO and EO information.

For the Rhone glacier, subsets of a 2010 digital terrain model (DTM) and a very-high resolution orthoimage were provided by the Swiss Federal Research Institute WSL. The color infrared (CIR) orthoimage has a resolution of 0.5 m. The DTM has a resolution of 1 m with a RMSE of 0.81 m (Ginzler and Hobi, 2015).

The DEM and orthoimagery for Svalbard is freely available through the Norwegian Polar Institute's (NPI) Geodata portal (geodata.npolar.no). The DEM of the area, NP_S0_DTM5_2010_13828_33 is a 5 m resolution DEM generated from high-resolution aerial imagery taken during a 2010 campaign. It was cropped down to include our area of interest which is roughly within the white dashed border in Figure 1. The standard deviation of the model is between 2-5 m (NPI, 2014).

The DEM for the Khumbu glacier was generated from very-high resolution Pleiades satellite imagery acquired on 7th October 2015. The 2015 model generation was done using only the supplied rational polynomial coefficients without GCPs. This is not an issue because we only wish to co-register the two models and are not looking for real world positioning accuracy. The resulting DEM and orthoimage have resolutions of 1 and 0.5 m respectively.

Model Generation

We used Agisoft Photoscan™ SfM software package version 1.1.6 build 2038- 1.2.5 build 22735 (64 bit) to create our DEMs. The processing was performed on a custom-built laptop running an Intel© Core™ i7-6700 4.00 GHz with eight cores and 64Gb of memory. The computer GPU is a NVIDIA® GeForce® GTX 980M with 8.0GB DDR5 Video RAM.

For each specific study site, images are first imported into Photoscan and areas that are not modelled are masked out using the mask tool. For the Rhone glacier imagery, masked areas include foreground as well as the horizon and mountains beyond the glacier area. For images from the Ny Ålesund survey, these areas mainly include features behind the first mountain ridge-line parallel to the flight path (i.e. limited line of sight areas) and the ocean shore line and sky. For the Khumbu glacier imagery these masked areas include the horizon, the watermarked edge of the photos as well as parts of the airplane that are present in some images.

Photoscan processing settings for each site are given in Table 1 below. Initial alignment was done at the setting of 'high' (i.e. normal resolution of imagery) for the Ny Ålesund imagery, 'highest' (i.e. upscaled by a factor of 4) for the Rhone and 'medium' (i.e. downscaled by a factor of 4) for the Khumbu imagery. No previously known camera information was used for our model generation (e.g. focal length) however the resulting estimated IO/EO data allow us to check estimate accuracy. The sparse point clouds generated for the three sites have 11662 (Rhone), 58742 (Ny Ålesund) and 18082 (Khumbu) points prior to filtering. Sparse points were filtered using the *Gradual Filter* function and any points with reprojection errors of greater than ~1 pix were removed, along with points that appear distant or obviously erroneous. This step is recommended in the Agisoft manual to help improve the accuracy of the following optimization steps and bundle adjustments by removing points with larger potential error (Agisoft, 2014). The resulting sparse point clouds contained 10370 (Rhone), 33657 (Ny Ålesund) and 5610 (Khumbu) points.

GCPs used to georeference point clouds were features identified in both the historic and current imagery that are unlikely to have changed positioning (e.g. large boulders on apparently stable terrain). Adding GCPs after initial alignment is

substantially faster than prior to alignment because the software can automatically determine the location of the GCP in each image used to construct the model after the user places the first marker. The software then populates the marker throughout the image data set. Following the placement of the first marker, we then filtered the photos to those with the marker and then adjusted the locations slightly to improve the placement accuracy. After each marker was positioned correctly, we entered the X, Y, Z data extracted from the current DEM and performed a bundle adjustment. We developed a method to speed up the identification of potential GCPs by placing perhaps 3-4 GCPs, spread out over the AOI, optimizing, then generating a dense cloud, a DEM and an orthophoto. It is then possible to drape the roughly aligned orthophoto over the current orthophoto and, using for example the swipe feature in ESRI's ArcMap, easily identify objects which have undergone no visible change. For Rhone glacier, Ny Ålesund and Khumbu glacier, 14, 27 and 32 GCPs were identified respectively.

After we identified all GCPs and performed model optimizations, we generated dense point clouds at high settings with moderate to aggressive point filtering. The dense point clouds for each site contained 1418606 (1.3 pts m^{-2}) (Rhone), 20053599 (1.8 pts m^{-2}) (Ny Ålesund) and 12563679 (1.7 pts m^{-2}) (Khumbu) points. Each dense cloud was then edited and points far beyond our areas of interest were removed along with obvious erroneous points.

Meshes were generated for the Rhone glacier and Ny Ålesund sites and smoothed using the Photoscan mesh tool, with a value of 3 for "passes", effectively acting as a high-pass filter to remove noise. This helped to smooth areas where automated dense point removal was difficult due to topography. For both the Rhone and Ny Ålesund sites, the resulting mesh was then used for DEM construction. For the

Khumbu glacier, however, the dense point cloud was easily editable and showed no signs of extreme noise, therefore we use the dense point cloud as the source for the final DEM. Generation of DEM with the setting "interpolated" enabled resulted in areas of over interpolation occurring around the model perimeter and in areas of poor visibility (e.g. behind ridges). After final DEMs were generated we produced the resulting orthoimagery using the DEMs as the underlying surface.

Calculated Focal Lengths and GSD

Upon completion of our DEM and orthoimagery generation it is possible to use the estimated IO and EO parameters, in combination with previous knowledge of image size and sensor size (i.e. film size), to calculate image focal lengths and fields of view for comparison. This information also aids us in determining potential maximum and minimum ground sampling distance (GSD).

To calculate the estimated focal length of the images in mm we take the estimated focal lengths in pixels, fp, divided by the corresponding pixel dimension of the image (i.e. width or height), p_w, and multiply by the actual sensor dimension (e.g. 35 mm film sensor has a 0.036 m width), s_w.

$$f_l = \frac{f_p}{p_w} s_w$$

Photoscan's camera data export gives two focal lengths, one for the horizontal dimension and one for the vertical. We have used the mean of the calculated focal lengths for each dimension. To calculate the horizontal and vertical fields of view we use the formulae (Wolf and Dewitt, 2000),

$$fov_H = 2\tan^{-1}\left(0.5\frac{s_w}{f_l}\right) \qquad\qquad fov_V = 2\tan^{-1}\left(0.5\frac{s_h}{f_l}\right)$$

Where fov_H, fov_V, s_w and s_h are the horizontal and vertical fields of view and the sensor width and height, respectively. We used sensor widths and heights of 0.12 x 0.09 m, 0.18 x 0.18 m and 0.036 x 0.024 m for the Rhone, Ny Ålesund and Khumbu imagery, respectively.

Using the camera EO and the calculated fields of view we then calculated the viewshed of each camera. This is similar to the viewshed tool in GIS software packages such as ESRI ArcMap, however we have added a calculation of the distance to each visible DEM pixel from the camera location as well. These distances were then used to calculate an estimated mean GSD map for each study site.

Results

DEM Error Analysis

The details of the resulting DEM and orthoimages generated through a SfM process are given in Table 2. The final resolutions of the DEMs for the Rhone, Ny Ålesund and the Khumbu glacier are 1.00, 2.30 and 1.44 m respectively. From the used GCPs for each site, the 3D RMSE are 7.24, 13.40 and 8.46 m however the RMSE in the Z direction are 3.11, 4.40 and 2.02 m respectively.

After differencing each DEM with the more recent DEMs, we masked out the glacier areas and calculated the RMSE of the off-glacier differences (ΔZ), which we assume should have a value of zero if the stable landscape has undergone no change. The ΔZ RMSE for the Rhone area is 2.62 m (mean -2.6 m) while the areas around Ny Ålesund and Khumbu are 0.57 m (mean -0.2 m) and 1.69 m (mean 1.6 m) respectively.

To determine the best possible standard deviation to use for our DEM differencing we analyzed the spread of off-glacier ΔZ values for each site. The results of this analysis are shown in Table 3 and Figure 3. The maximum and minimum off-glacier ΔZ for the Rhone glacier, Ny Ålesund and the Khumbu glacier are 46.4, 136.2 and 32.9 m (max) and -78.1, -355.3 and -40.1 m (min), respectively. While these values seem quite large, the interquartile range of off-glacier ΔZ (i.e. minimum and maximum of the middle 50% of the data) for each site is between -4.4 – 1.3 m (Rhone), -3.0 – 2.7 m (Ny Ålesund) and -1.0 – 3.0 m (Khumbu) (Table 3).

Outliers in each set of off-glacier ΔZ are given as values within 1.5σ to 3σ away from the interquartile boundaries. Extreme outliers on the other hand are classified as being greater than 3σ away from the interquartile boundaries (Table 3) and make up a very small percentage of the overall off-glacier ΔZ (Figure 3). For the Rhone site the outliers make up 8.9% of the total sampled off-glacier ΔZ. For the Ny Ålesund and Khumbu sites the outliers make up 10.5% and 3.0% respectively (Figure 3). To visually inspect the spatial distribution of both normal and extreme outliers we removed all non-outlier data from the set and draped a raster layer over the DEMs in a GIS environment. We displayed outliers as grey and extreme outliers as black (Figures 4, 5 and 6, C). These areas show up in either zones of poor photographic coverage or along the edges of our study areas and can be identified as over interpolation artifacts from Photoscan. Taking this into consideration, we removed all the data considered extreme outliers and recalculated our off-glacier ΔZ statistics. Our original ΔZσ, including extreme outliers, were ±9.5 m, 18.1 m and 3.5 m, and excluding these outliers ±5.4 m, 5.2 m and 3.3 m for the Rhone glacier, Ny Ålesund and the Khumbu Glacier respectively (Table 2).

Final Products

Our resulting orthoimages, DEMs and differences are shown in Figures 4, 5 and 6. The resolution of the orthoimagery, as stated by Photoscan during export, are 0.2 m,1.0 m and 0.5 m for the Rhone glacier, Ny Ålesund and the Khumbu glacier respectively. The Ny Ålesund orthoimage does have some gaps and blurred areas that occur beyond the mountain ridge running parallel to the flight direction (i.e. west to east). The Rhone glacier image also shows some blurred areas, which we can attribute to areas with poor coverage and a lower number of final points. These areas of sparse coverage cause excessive stretching of the orthoimagery during final mosaicking. The distribution of GCPs is shown in Figures 4, 5 and 6 as yellow markers overlain on the orthoimages.

The hillshaded DEMs (Figures 4, 5 and 6, B) show a high amount of detail and do not appear to contain any extremely erroneous points in the areas of interest. The upper edge and lower right corner of the Rhone DEM (Figure 4, B), as well as the southern side of the Ny Ålesund (Figure 5, B) and Khumbu (Figure 6, B) DEMs, contain the areas previously mentioned as zones of poor coverage and over interpolation. The Ny Ålesund DEM suffers from numerous areas of over interpolation and gaps due to poor reconstruction, or of little to no visibility being interpolated across. We were able to easily identify the largest of these areas in the hillshaded DEM and removed them prior to differencing.

The differenced DEMs (Figures 4, 5 and 6, C) show very distinct patterns of glacier mass loss for each of our study sites. The color maps for each have been adjusted to show areas within the calculated standard deviation (e.g. ±5.4, 5.2 and 3.3 m) as well as the remaining areas. This makes it easier to see that in the off-glacier regions

of each site our differencing appears to be within these errors. The calculated levels of detection as shown in Lane et al. (2003), at the 68% confidence limit, are 5.4, 5.6 and 3.6 m for the Rhone, Ny Ålesund and Khumbu sites respectively. The limit of -15 m change was chosen since in some areas we have deposition as opposed to lowering, a process that we mainly observed on the Khumbu glacier (Figure 6, C). For each difference map, the regions colored grey or black represent the outlier and extreme outlier areas respectively. For the Rhone glacier, these areas occur along corners of the DEM, whereas in Ny Ålesund many of these areas occur on the southern edge and on slopes that were shaded or occurred in areas of poor visibility. For the Khumbu glacier, these areas are located at the end of the terminus and are most likely due to shading on hillsides or areas where the surface material is over exposed and extremely bright, which again would lead to poor contrast and texture.

Elevation Profiles

We have extracted elevation profiles (black lines in Figures 4, 5 and 6 C) from each site to assess the detailed surface data as well as compare previous glacier surfaces to recent data (Figure 7). For the Ny Ålesund site, we have chosen 5 glaciers. From west to east, these glaciers are Vestre Brøggerbreen, Austre Brøggerbreen, Midtre Lovénbreen, Austre Lovénbreen and Pedersenbreen (Figure 5, C).

Focal Lengths and Ground Sampling Distance (GSD)

In order to constrain the potential DEM resolutions we could achieve using oblique and high-oblique imagery, we calculated the estimated mean ground sampling distance (GSD) based on the final estimated camera IO and EO information. As mentioned previously, it was possible to calculate the focal lengths of each image based on the estimated IO parameters and knowledge of the camera sensor size.

Though we know the focal length of the imagery from Ny Ålesund, we decided to not use it for model generation and therefore assess how well the software could estimate it based on the GCP data.

The Rhone glacier imagery, which was taken on a 9x12 cm plate camera, is estimated to have been taken with a mean focal length of 147±2.6 mm. The Ny Ålesund imagery, taken on an 18x18 cm film, is estimated to have been taken with a mean focal length of 208±1.2 mm, only 2 mm less than the given focal length. The Khumbu imagery on the other hand, taken on 35 mm film by multiple persons, shows numerous focal lengths, which is ultimately why we chose to not group the photos together (Figure 8). There are clusters of images that appear generally consistent, such as images from GF14, which have a mean focal length of 33±1.3 mm and likewise with images from GY01 which have a mean focal length 60±3.8 mm. Photographs from the GN07 have a large spread of focal lengths and, in fact, many of these photos appear to be zoomed in on smaller areas when compared to those of the GF or GY series.

Using these focal length data in the field of view formulae, we find the Rhone imagery has a 44° horizontal and 34° vertical field of view. This was verified by manually identifying objects near the horizontal and vertical edges of the images, and matching these with objects in the 2010 orthoimage. We calculated a horizontal FOV of 43.8° and a vertical FOV of 33.9° based on the angle made by these points and the estimate camera locations. The fields of view for the Ny Ålesund imagery are 46° for both the horizontal and vertical. The Khumbu imagery, being a mixture of focal lengths, shows mean horizontal and vertical fields of view of 59° and 41° for the GF14 imagery, 35° and 24° for the GY01 images and variable field of view for the GY07 and GN07 imagery.

The estimated mean GSD calculated using the camera locations as well as the calculated fields of view is shown in Figure 9. For all three sites the GSD decreases with increasing distance from the cameras yet for our image resolutions and camera positions, our areas of interest all have potentially high GSD. For the Rhone glacier, the GSD ranges from 0.18-0.52 m pix^{-1} (Figure 9, A), which, when investigating the photographs appears to be accurate as it is possible to make out the window frames of the Hotel Belvédère, on the far mountain ridge. These frames are made up of 1-3 pixels and, at 0.5 m pix^{-1}, this results in a realistic window frame size. In the nearer foreground of one picture, we can see a small hut and two figures on the very edge of the glacier. The figures are roughly 6 pixels high, which in this area with a GSD of 0.25-0.30 m pix^{-1} would amount to persons with heights of 1.5-1.8 m.

In Ny Ålesund the GSD ranges from 1.32-2.87 m pix^{-1} (Figure 9, B). Differencing the 5 m 2010 DEM from the 1936 DEM reveals patterns of surface drainage on glaciers that could be meltwater channels with widths and depths within these GSD ranges. The furthest away mountain ridge, within our area of interest has a GSD of maximum ~2.5 m pix^{-1}. Image quality of those distant areas is quite low, however, and often lacks texture and contrast, making it difficult to pinpoint potential GCPs from the imagery.

The Khumbu glacier GSD ranges from 0.36-0.90 m pix^{-1}, based on the average focal length coverage per pixel (Figure 9, C). The area in the central part of the glacier tongue has the best GSD as the GY01 photographs were taken in a circular pattern above this area at a focal length of ~60 mm at near nadir. Many of the other parts of the area are covered with wither few large focal length images or many wide angle, ~33 mm focal length images from a distance.

Observations

All three glaciers experienced significant retreat and/or downwasting over the respective periods of observation. The lower Rhone glacier has completely disappeared from the study area. Of the five Ny Ålesund glaciers, four exhibit a similar pattern of retreat and strong downwasting at the terminus, with less surface lowering up glacier. In contrast, Austre Lovénbreen exhibits significant downwasting over the whole area of investigation. Although the pattern of downwasting on the Khumbu glacier exhibits extreme heterogeneity, little downwasting is evident in the terminus regions with high downwasting rate displaced upglacier.

The Rhone glacier terminus transitioned from an elevation of 1790 m a.s.l. to ~2210 m a.s.l. The elevation profile shows the maximum thinning along the centerline was located at the foot of the steep underlying valley wall (Figure 7, A). Discharge from the glacier exited at the concave wall located in the center of the terminus (Figure 4, B, black circle, Figure 10). Upglacier from this feature there are two surface depressions running along the glacier length (Figure 4, B, dashed lines). To the west this depression occurs in a highly-crevassed region, while to the east it occurs below a crevassed region and contains a surface meltwater channel which exits the surface only a few meters to the east of the observed subglacial drainage. Since the early 1980s the terminus has retreated another 375 m. The melting of the lower Rhone glacier removed roughly $18.5*10^7 \pm 0.2*10^7$ m^3 of ice over an area of $4.05*10^5$ m^2. Over the period of 1896-1980 this amount of melt would correspond to an annual surface lowering of 0.54 m/y in the lower tongue.

The five glaciers in Ny Ålesund all show similar patterns of surface lowering, with localized accentuated lowering in the central terminus region followed by a gradual

decrease in lowering up glacier (Figure 5, C & Figure 7 B-F). Austre Lovénbreen, however, displays a much more pronounced overall thinning pattern where the measured thinning, 3 km from the 1936 terminus, is still ~69±5.2 m, in contrast to a mean of 25±5.2 m for the other glaciers. Vestre and Austre Brøggerbreen show peak melting along the transects of 71 m and 85±5.2 m respectively, whereas the remaining three glaciers show values of 92 m, 94 m and 93±5.2 m for Midtre Lovénbreen, Austre Lovénbreen and Pedersenbreen respectively (Figure 7, B-F). The maximum thinning rates from 1936-2010, along the transects are 0.96 m a^{-1}, 1.14 m a^{-1}, 1.24 m a^{-1}, 1.27 m a^{-1} and 1.26±0.07 m a^{-1}, with mean thinning rates of 0.31 m a^{-1}, 0.48 m a^{-1}, 0.51 m a^{-1}, 0.86 m a^{-1} and 0.65 m a^{-1} from west to east respectively.

Nuth et al. (2007) constructed a DEM for a large portion of Svalbard based on 50 m contour lines extracted from the 1938 topographic map of Svalbard which is based on the aerial oblique imagery of 1936 and 1938. Their DEM was differenced with the 1990 DEM, NP_S0_DTM20_199095_33, which has a 20 m resolution with a horizontal accuracy of ±2-3 m (NPI, 2014). We have differenced our Ny Ålesund with the 1990 DEM and calculated the average elevation changes curves of our five glaciers. Our values fit closely with the average values of Prins Karls Forland and Brøggerhalvøya (Figure 11). The accuracy of the values in the 400-500 m altitudes are questionable as there may be influences from over interpolated edges, however, as a comparison, our data fits well with the previously calculated data.

While the Rhone glacier and the glaciers in the Ny Ålesund area are clean ice glaciers, which, exhibit relatively smooth elevation profiles and similar thinning profiles (Figure 7), the Khumbu glacier is a highly debris-covered glacier which exhibits hummocky topography and highly variable spatial thinning patterns (Figure 6

B and C). The lower 1 km of the Khumbu appears to have undergone very little change over the 37-year period, showing average thinning along the transect of 7.5±3.3 m. Upglacier from here the difference map demonstrates large variability in spatial patterns of downwasting with a maximum of 64.1±3.3 m, a minimum of -12.5±3.3 m and a mean thinning of 28.6±3.3 m.

The high degree of spatial variability in downwasting rates reflects the critical control of debris thickness on melt rates. Where debris layer thickness exceeds a few 10s of cm, little sub-debris melt can occur (Nakawo and Rana, 1999, Nicholson and Benn, 2006, Reznichenko et al., 2010). Consequently, non-uniform debris distributions create heterogeneous melt patterns that result in uneven, hummocky surface topography (e.g. Figure 6, B; Figure 12, dotted line). Thick accumulations of debris at down-glacier sites have resulted in limited to no downwasting. Further upglacier, thinner and more partial debris cover allows rapid, patchy downwasting in hot spots due to debris redistribution. Areas with steep surface slopes can increase, material can be redistributed through slumping, newly exposed ice can melt rapidly, increased surface meltwater production can lead to pond and lake formation, and subsequent lake margin calving can cause rapid backwasting of exposed ice faces (Watanabe et al., 1986, Sakai et al., 2000, Benn et al., 2001, Gulley and Benn, 2007, Röhl, 2008, Reid and Brock, 2014, Thompson et al., 2016).

Despite the large range of melt rates, mean thinning for the 2.77 km^2 area is 19.8±3.3 m, which is similar to the mean thinning of the total ablation area between 1970-2007, of 13.9±2.5 m (Bolch et al., 2011). This corresponds to a mean thinning rate of 0.54±0.9 m a^{-1} for the terminus region.

In summary, we have demonstrated how, through the use of historic imagery and modern remote sensing products, it is possible to extract reliable, high resolution DEMs and orthoimagery of glaciers from 38, 80 and 120 years ago. By searching through online databases for overlapping imagery of glaciers, even with a minimum of 3 photos (in the Rhone glacier case) it is possible to extract high quality geometric information using SfM technology. We have shown that the method can successfully extract the data and, if given enough reliable GCPs, its can also estimate the camera IO and EO information. Our analysis of off-glacier error shows that the method produces accurate DEMs within the areas visible from numerous cameras and that relative to the timespans between the historic imagery and the current imagery, the errors are small. Using the estimated IO and EO information we have been able to calculate estimated potential maximum GSDs, which, even when using aerial high-oblique imagery, can be on the order of ~2-3 m or less. Our DEM differencing shows trends similar to numerous other studies and measurements performed in our selected regions. Elevation profiles from our glaciers demonstrates how differently glaciers from the high Arctic, European Alps and the Himalayas, both clean and debris-covered, have responded to the warming climate over the last ~40-100 years.

Discussion

Our results demonstrate the potential for using historical imagery to create DEMs of numerous glaciated regions including alpine glaciers, high arctic clean ice glaciers and heavily debris-covered Himalayan glaciers, using a variety of imagery from numerous time periods. Here we present details about the quality of our resulting DEMs and orthoimages and offer possible explanations for erroneous areas. Finally, we use the observed changes between the earlier DEMs and the more recent DEMs

to discuss differences in the patterns of long term glacier surface change at the three sites.

DEMs and Orthophotos

For all study sites the spatial distribution of off-glacier DEM differences appears largely uniform, within the limits of our calculated ΔZσ. The ΔZσ of ±5.4, 5.2, and 3.3 m for the Rhone glacier, Ny Ålesund and the Khumbu glacier respectively, and represent percentage errors as small as ~5% in the areas of greatest change. However, through the use of the Matlab script sfm_georef (v3.1, James and Robson, 2012, James et al., 2017) we have been able to detect what could be considered "doming" or systematic error as discussed in James and Robson (2014) and James et al. (2017) and determine what improvements can be made by removing GCP outliers. The amplitudes of doming are on the scale of ±~6 m over a distance of 9 km in Ny Ålesund (minimized to ±~4 m with the removal of the five GCPs with highest residuals), roughly +6 to -8 m over a distance of 1 km at the Rhone (minimized to ±~3 m with the removal of the two GCPs with the highest residuals), and roughly +3 to -5 over a distance of 4 km at the Khumbu (minimized to ±2.5 m with the removal of the three GCPs with the highest residuals).

Aside from the removal of GCPs with the highest residuals, a further step would be to improve the accuracy of the self-calibrated K1 value (James and Robson, 2014) through the iterative use of sfm_georef and the doming analysis tool (v3.1 James and Robson, 2012). Yet due to the ungrouped nature of the photos used for both the Rhone and the Khumbu this method would be quite time consuming as each individual image would have to be adjusted separately from the rest, moving from a single degree of freedom to multiple (personal communication with Prof. James).

In comparison to qualities of other SfM derived DEMs, our results appear to fit closely to the relationship between photograph range and model RMSE (Smith and Vericat, 2015). In a similar study by Midgley and Tonkin (2017), a DEM of Austre and Midtre Lovénbreen was derived from three of the 1936 NPI high-oblique aerial images using SfM. They derived 7 GCPs from a high-resolution (~1.15 points/m^2) LiDAR derived DEM (Barrand et al., 2009) enabling them to generate a DEM with an error of ±5 m. Our errors, being only slightly larger than those found by Midgley and Tonkin (2017) are very promising considering that we were not using high precision GCPs and we were limited by the accuracy, resolution and error of our source DEM (e.g. 5x5 m resolution, ±2-3 m error in Brøggerhalvøya).

The generated orthophotos and DEMs for all three sites are of sufficiently high quality and resolution to detect changes in the glacier surfaces over the sampled time intervals both through visual inspection and DEM differencing. Removing areas that statistically represent outliers, we can also remove sections of the orthoimages where over interpolation causes extreme image warping. Our end results are, in most cases, smooth orthoimages that appear very closely aligned to our more recent current orthoimagery.

The DEMs for all three locations appear to have only small areas of questionable quality. By viewing the DEMs with a hillshade overlay it becomes easier to identify the interpolated regions along edges as coinciding with areas of limited visibility (e.g. behind Ny Ålesund mountains). The Khumbu glacier DEM shows some signs of noise in the lower and upper sections of the DEM. As the majority of the images used were taken above the central region, it is not unexpected that the upper and lower sections should have more noise, they may have 6-8 image overlap, but much of it is from similar viewpoints, with greater distances between the ground and

cameras. The detected points in these two areas may therefore have a higher reconstruction uncertainty, such as previously mentioned for the Rhone glacier.

Aside from poor reconstruction in areas of limited camera coverage or high viewing angles, the only other areas where there was difficulty extracting data were in locations with poor lighting or limited contrast. Many of the mountainsides in the Ny Ålesund DEM have vertical gullies running downslope which cause alternating light and dark surfaces under the oblique sun angle. Positional errors on hillslopes can lead to higher Z error due to the fact that a horizontal difference in one direction creates a vertical difference dependent on the slope angle (Nuth and Kääb, 2011).

While the Ny Ålesund and Khumbu DEMs provide nearly complete spatial coverage across the glaciers, the Rhone glacier DEM exhibits interpolation errors that are unique to its image dataset. For example, the DEM suffers from numerous areas of warping that are most likely caused by the terrestrial aspect of the camera position and the angle of the glacier surface. These highly oblique angles mean that some portions of the glacier are hidden from view in shadows, such as the area behind a large rock or ice block, and the model interpolates over and stretches the images in these shadowed regions. However, viewing the scene from the perspective of a person on the ground, these areas are not visible, and the scene itself appears to be of high quality (Figure 10). In addition to the camera position of Rhone imagery, the older acquisition date of 1896, means the image quality is lower, due to increased noise from ageing and lack of detail and contrast, contributing to fewer matched features. Of the series of Rhone glacier images taken in 1896, these three images are the only ones that we could successfully align, but using only three images is not an ideal situation as it limits the number and quality of the points matched between

image pairs. Perhaps with more than three images, the maximum reconstruction uncertainty would decrease.

Despite the limitations discussed above, using archived photographs as a data source for SfM surface model generation can provide valuable information. For the purpose of studying changes in glacier surface patterns over very long time intervals, our results have a small percentage error in relation to the changes detected and can offer an excellent opportunity to extend the time series of glacier observations back beyond the current period of abundant data sets, providing context to higher temporal resolution recent assessments of glacier surface change and also providing insights into glacier behavior over longer timescales.

Conclusion

Our results demonstrate that using SfM to create DEMs from historical images offers a powerful new tool for characterizing patterns of glacier downwasting. DEMs constructed from historical imagery can fill in gaps where no other remotely sensed, or field data exist. In the case of the Rhone glacier, the temporal coverage of the repeated photographs means it could be possible to reconstruct multiple DEMs of the lower Rhone and more accurately measure the disintegration of the glacier tongue from the late 1800s through ~1980. It would be possible to create models with detail such as shown in Figure 10 and animate the retreat of the terminus up the valley wall. Older oblique imagery can now be successfully used to extract DEMs of objects in the foreground. Terrestrial imagery can also be used, so long as there is sufficient coverage of off-glacier areas to identify GCPs. Even using mixed focal lengths can still yield high quality results suitable for observing glacial change. The application of SfM to such imagery can not only unlock the past and contribute to a

better understanding of current and future trends in glacier climate interactions, but it can also help to increase knowledge on the development and evolution of debris-covered glaciers. By allowing us to better understand how and at what rates, surface processes occur we can develop a better sequence behind the glacier surfaces we see today, and more accurately forecast how the surface will evolve in the future.

References

Agarwal S, Furukawa Y, Snavely N, Simon I, Curless B, Seitz SM, Szeliski R. 2011. Building rome in a day. Communications of the ACM **54**: 105-112

Agisoft, 2014. Agisoft PhotoScan User Manual. In *Professional Edition, Version 1*. Agisoft LLC: http://www.agisoft.ru/pdf/photoscan_pro_1_0_en.pdfhttp://www.agisoft.ru/pdf/photoscan_pro_1_0_en.pdf, http://www.agisoft.ru/pdf/photoscan_pro_1_0_en.pdf

Baltsavias EP, Favey E, Bauder A, Bosch H, Pateraki M. 2001. Digital surface modelling by airborne laser scanning and digital photogrammetry for glacier monitoring. The Photogrammetric Record **17**: 243-273

Barrand NE, James TD, Murray T. 2010. Spatio-temporal variability in elevation changes of two high-Arctic valley glaciers. Journal of Glaciology **56**: 771-780

Barrand NE, Murray T, James TD, Barr SL, Mills JP. 2009. Optimizing photogrammetric DEMs for glacier volume change assessment using laser-scanning derived ground-control points. Journal of Glaciology **55**: 106-116

Benn DI, Wiseman S, Hands KA. 2001. Growth and drainage of supraglacial lakes on debrismantled Ngozumpa Glacier, Khumbu Himal, Nepal. Journal of Glaciology **47**: 626-638. DOI: 10.3189/172756501781831729

Bhambri R, Bolch T, Chaujar RK, Kulshreshtha SC. 2011. Glacier changes in the Garhwal Himalaya, India, from 1968 to 2006 based on remote sensing. Journal of Glaciology **57**: 543-556. DOI: 10.3189/002214311796905604

Bhardwaj A, Sam L, Bhardwaj A, Martín-Torres FJ. 2016a. LiDAR remote sensing of the cryosphere: Present applications and future prospects. Remote Sensing of Environment **177**: 125-143. DOI: 10.1016/j.rse.2016.02.031

Bhardwaj A, Sam L, Martín-Torres FJ, Kumar R. 2016b. UAVs as remote sensing platform in glaciology: Present applications and future prospects. Remote Sensing of Environment **175**: 196-204. DOI: 10.1016/j.rse.2015.12.029

Bjork AA, Kjaer KH, Korsgaard NJ, Khan SA, Kjeldsen KK, Andresen CS, Box JE, Larsen NK, Funder S. 2012. An aerial view of 80 years of climate-related glacier fluctuations in southeast Greenland. Nature Geosci **5**: 427-432. DOI: http://www.nature.com/ngeo/journal/v5/n6/abs/ngeo1481.html#supplementary-information

Bolch T, Pieczonka T, Benn D. 2011. Multi-decadal mass loss of glaciers in the Everest area (Nepal Himalaya) derived from stereo imagery. The Cryosphere **5**: 349-358. DOI: 10.5194/tc-5-349-2011

Braithwaite RJ, Raper SC, Candela R. 2013. Recent changes (1991–2010) in glacier mass balance and air temperature in the European Alps. Annals of Glaciology **54**: 139-146. DOI: 10.3189/2013AoG63A285

Carter HA. 1985. Classification of the Himalaya. American Alpine Journal **27**: 122-123

Debenham F. 1938. Norwegian Expedition to Svalbard, 1938. Polar Record **3**: 5-6. DOI: 10.1017/S003224740003802X

Diolaiuti G, Bocchiola D, D'agata C, Smiraglia C. 2012. Evidence of climate change impact upon glaciers' recession within the Italian Alps. Theoretical and Applied Climatology **109**: 429-445. DOI: 10.1007/s00704-012-0589-y

ETH-Bibliothek. 2016. Rhonegletscher 30-Aug-1896. In *Glaziologische Kommission der SANW (Archiv)*, e-pics Online Database. ETH Bibliothek: Zurich. http://www.e-pics.ethz.ch/. DOI: http://goi.org/10.3932/ethz-a-000016893

http://goi.org/10.3932/ethz-a-000016894

http://goi.org/10.3932/ethz-a-000016896

Fleming KM, Dowdeswell JA, Oerlemans J. 1997. Modelling the mass balance of northwest Spitsbergen glaciers and responses to climate change. Annals of Glaciology **24**: 203-210

Gabbud C, Micheletti N, Lane SN. 2016. Response of a temperate Alpine valley glacier to climate change at the decadal scale. Geografiska Annaler: Series A, Physical Geography **98**: 81-95

Ginzler C, Hobi ML. 2015. Countrywide stereo-image matching for updating digital surface models in the framework of the Swiss national forest inventory. Remote Sensing **7**: 4343-4370

Gruen A, Murai S. 2002. High-resolution 3D modelling and visualization of Mount Everest. ISPRS journal of photogrammetry and remote sensing **57**: 102-113

Gulley J, Benn DI. 2007. Structural control of englacial drainage systems in Himalayan debris-covered glaciers. Journal of Glaciology **53**: 399-412. DOI: 10.3189/002214307783258378

Haeberli W, Kääb A, Mühll DV, Teysseire P. 2001. Prevention of outburst floods from periglacial lakes at Grubengletscher, Valais, Swiss Alps. Journal of Glaciology **47**: 111-122. DOI: 10.3189/172756501781832575

Hagen JO, Kohler J, Melvold K, Winther JG. 2003. Glaciers in Svalbard: mass balance, runoff and freshwater flux. Polar Research **22**: 145-159

Immerzeel WW, van Beek LP, Bierkens MF. 2010. Climate change will affect the Asian water towers. Science **328**: 1382-1385

James M, Robson S. 2012. Straightforward reconstruction of 3D surfaces and topography with a camera: Accuracy and geoscience application. Journal of Geophysical Research: Earth Surface **117**:

James MR, Robson S. 2014. Mitigating systematic error in topographic models derived from UAV and ground-based image networks. Earth Surface Processes and Landforms **39**: 1413-1420

James MR, Robson S, d'Oleire-Oltmanns S, Niethammer U. 2017. Optimising UAV topographic surveys processed with structure-from-motion: Ground control quality, quantity and bundle adjustment. Geomorphology **280**: 51-66. DOI: http://dx.doi.org/10.1016/j.geomorph.2016.11.021

Jon Ove H, Olav L. 1990. Long-Term Glacier Mass-Balance Investigations In Svalbard, 1950-88. Annals of Glaciology **14**: 102-106

Jouvet G, Huss M, Blatter H, Picasso M, Rappaz J. 2009. Numerical simulation of Rhonegletscher from 1874 to 2100. Journal of Computational Physics **228**: 6426-6439

Kääb A. 2000. Photogrammetric reconstruction of glacier mass balance using a kinematic ice-flow model: a 20 year time series on Grubengletscher, Swiss Alps. Annals of Glaciology **31**: 45-52

Kääb A, Funk M. 1999. Instruments and methods modelling mass balance using photogrammetric and geophysical data: a pilot study at Griesgletscher, Swiss Alps. Journal of Glaciology **45**: 575-583

Kamp U, Byrne M, Bolch T. 2011. Glacier fluctuations between 1975 and 2008 in the Greater Himalaya Range of Zanskar, southern Ladakh. Journal of Mountain Science **8**: 374-389. DOI: 10.1007/s11629-011-2007-9

Keutterling A, Thomas A. 2006. Monitoring glacier elevation and volume changes with digital photogrammetry and GIS at Gepatschferner glacier, Austria. International Journal of Remote Sensing **27**: 4371-4380

Kohler J, James T, Murray T, Nuth C, Brandt O, Barrand N, Aas H, Luckman A. 2007. Acceleration in thinning rate on western Svalbard glaciers. Geophysical Research Letters **34**:

Lane SN, Westaway RM, Murray Hicks D. 2003. Estimation of erosion and deposition volumes in a large, gravel-bed, braided river using synoptic remote sensing. Earth Surface Processes and Landforms **28**: 249-271

Lefauconnier B, Hagen JO, Ørbæk JB, Melvold K, Isaksson E. 1999. Glacier balance trends in the Kongsfjorden area, western Spitsbergen, Svalbard, in relation to the climate. Polar Research **18**: 307-313

López-Moreno JI, Fontaneda S, Bazo J, Revuelto J, Azorin-Molina C, Valero-Garcés B, Morán-Tejeda E, Vicente-Serrano SM, Zubieta R, Alejo-Cochachín J. 2014. Recent glacier retreat and climate trends in Cordillera Huaytapallana, Peru. Global and Planetary Change **112**: 1-11. DOI: 10.1016/j.gloplacha.2013.10.010

Mercanton P-L, Heim A, Held L, Rütimeyer L. 1916. Vermessungen am Rhonegletscher: Mensurations au glacier du Rhône. 1874-1915. Zürcher & Furrer

Midgley NG, Tonkin TN. 2017. Reconstruction of former glacier surface topography from archive oblique aerial images. Geomorphology **282**: 18-26

Nakawo M, Rana B. 1999. Estimate of Ablation Rate of Glacier Ice under a Supraglacial Debris Layer. Geografiska Annaler: Series A, Physical Geography **81**: 695-701. DOI: 10.1111/1468-0459.00097

Nakawo M, Yabuki H, Sakai A. 1999. Characteristics of Khumbu Glacier, Nepal Himalaya: recent change in the debris-covered area. Annals of Glaciology **28**: 118-122

Nicholson L, Benn DI. 2006. Calculating ice melt beneath a debris layer using meteorological data. Journal of Glaciology **52**: 463-470. DOI: 10.3189/172756506781828584

NPI. 2014. Terrengmodell Svalbard: NP_S0_DTM5_2010_13828_33. Tromso, Norway. https://data.npolar.no/dataset/dce53a47-c726-4845-85c3-a65b46fe2fea

Nuth C, Kääb A. 2011. Co-registration and bias corrections of satellite elevation data sets for quantifying glacier thickness change. The Cryosphere **5**: 271-290

Nuth C, Kohler J, Aas HF, Brandt O, Hagen JO. 2007. Glacier geometry and elevation changes on Svalbard (1936-90): a baseline dataset. Annals of Glaciology **46**: 106-116. DOI: 10.3189/172756407782871440

Paul F, Kääb A, Haeberli W. 2007. Recent glacier changes in the Alps observed by satellite: Consequences for future monitoring strategies. Global and Planetary Change **56**: 111-122. DOI: 10.1016/j.gloplacha.2006.07.001

Quincey DJ, Luckman A, Benn D. 2009. Quantification of Everest region glacier velocities between 1992 and 2002, using satellite radar interferometry and feature tracking. Journal of Glaciology **55**: 596-606. DOI: 10.3189/002214309789470987

Reid T, Brock B. 2014. Assessing ice-cliff backwasting and its contribution to total ablation of debris-covered Miage glacier, Mont Blanc massif, Italy. Journal of Glaciology **60**: 3. DOI: 10.3189/2014JoG13J045

Reznichenko N, Davies T, Shulmeister J, McSaveney M. 2010. Effects of debris on ice-surface melting rates: an experimental study. Journal of Glaciology **56**: 384-394. DOI: 10.3189/002214310792447725

Roderik JW, Van De Wal S. 1998. Sensitivity of Rhonegletscher, Switzerland, to climate change: experiments with a one-dimensional flowline model. Journal of Glaciology **44**: 383-393

Röhl K. 2008. Characteristics and evolution of supraglacial ponds on debris-covered Tasman Glacier, New Zealand. Journal of Glaciology **54**: 867-880. DOI: 10.3189/002214308787779861

Sakai A, Takeuchi N, Fujita K, Nakawo M. 2000. Role of supraglacial ponds in the ablation process of a debris-covered glacier in the Nepal Himalayas. IAHS PUBLICATION: 119-132

Silverio W, Jaquet J-M. 2005. Glacial cover mapping (1987–1996) of the Cordillera Blanca (Peru) using satellite imagery. Remote Sensing of Environment **95**: 342-350. DOI: 10.1016/j.rse.2004.12.012

Smith MW, Vericat D. 2015. From experimental plots to experimental landscapes: topography, erosion and deposition in sub-humid badlands from Structure-from-Motion photogrammetry. Earth Surface Processes and Landforms **40**: 1656-1671

Soruco A, Vincent C, Rabatel A, Francou B, Thibert E, Sicart JE, Condom T. 2015. Contribution of glacier runoff to water resources of La Paz city, Bolivia (16 S). Annals of Glaciology **56**: 147-154. DOI: 10.3189/2015AoG70A001

Sugiyama S, Bauder A, Zahno C, Funk M. 2007. Evolution of Rhonegletscher, Switzerland, over the past 125 years and in the future: application of an improved flowline model. Annals of Glaciology **46**: 268-274

Surazakov A, Aizen V, Aizen E, Nikitin S. 2007. Glacier changes in the Siberian Altai Mountains, Ob river basin,(1952–2006) estimated with high resolution imagery. Environmental Research Letters **2**: 045017. DOI: 10.1088/1748-9326/2/4/045017

Thompson S, Benn DI, Mertes J, Luckman A. 2016. Stagnation and mass loss on a Himalayan debris-covered glacier: processes, patterns and rates. Journal of Glaciology: 1-19. DOI: 10.1017/jog.2016.37

Thorsteinsson T, Jóhannesson T, Snorrason Á. 2013. Glaciers and ice caps: Vulnerable water resources in a warming climate. Current Opinion in Environmental Sustainability **5**: 590-598. DOI: 10.1016/j.cosust.2013.11.003

Unger-Shayesteh K, Vorogushyn S, Farinotti D, Gafurov A, Duethmann D, Mandychev A, Merz B. 2013. What do we know about past changes in the water cycle of Central Asian headwaters? A review. Global and Planetary Change **110**: 4-25. DOI: 10.1016/j.gloplacha.2013.02.004

Wallinga J, Wal RSWVD. 1998. Sensitivity of Rhonegletscher, Switzerland, to climate change: experiments with a one-dimensional flowline model. Journal of Glaciology **44**: 383-393. DOI: 10.3198/1998JoG44-147-383-393

Wang S, Liu H, Yu B, Zhou G, Cheng X. 2016. Revealing the early ice flow patterns with historical Declassified Intelligence Satellite Photographs back to 1960s. Geophysical Research Letters **43**: 5758-5767. DOI: 10.1002/2016GL068990

Watanabe O, Iwata S, Fushimi H. 1986. Topographic characteristics in the ablation area of the Khumbu Glacier, Nepal Himalaya. Annals of Glaciology **8**: 177-180

Wiesmann S, Steiner L, Pozzi M, Bozzini C, Bauder A, Hurni L, 2012. Reconstructing historic glacier states based on terrestrial oblique photographs. In *Proceedings of the AutoCarto International Symposium on Automated Cartography, Columbus, OH, USA*, 1618,

Wolf PR, Dewitt BA. 2000. Elements of Photogrammetry: with applications in GIS. McGraw-Hill New York

Yabuki H, 2012. Aerial photographs of glaciers in Nepal Himalaya obtained during the Glaciological Expedition in Nepal from 1974 to 1978. CrDAP J, GEN-(Nagoya University, The Japanese Society of Snow and Ice) (ed). distributed by CrDAP, Digital media: Yokosuka, Japan
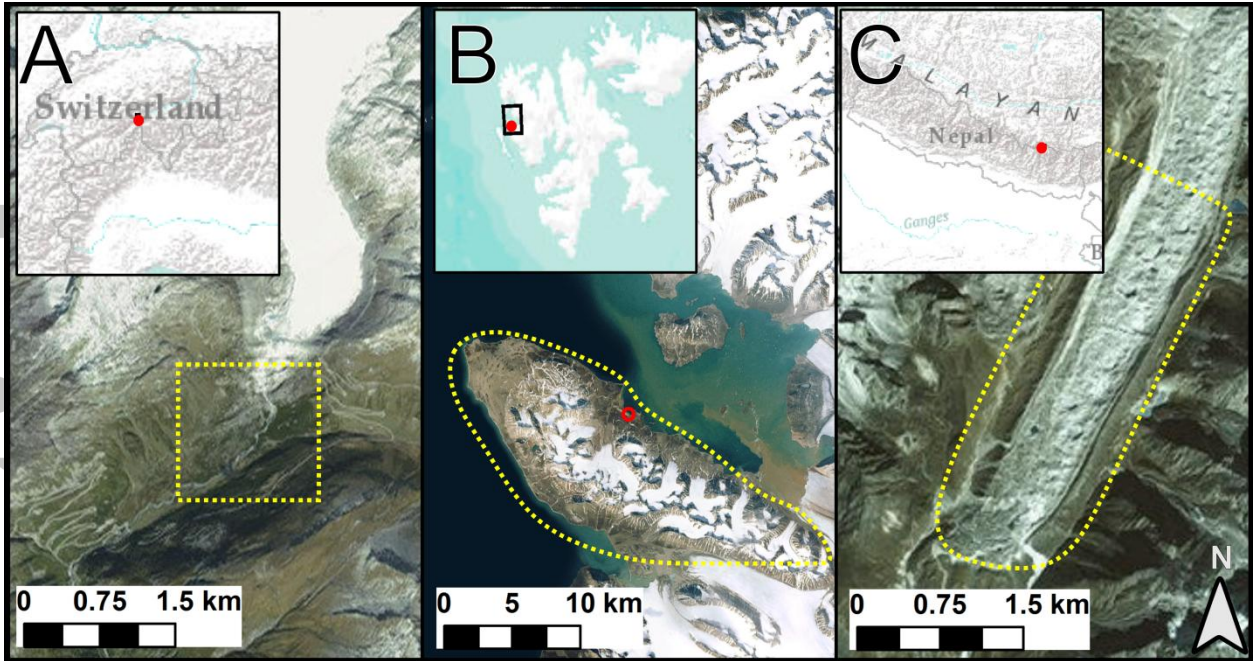
Figure 1: Overview of three study sites, A) lower Rhone glacier, Switzerland, B) Brøggerhaløya and Ny Ålesund (red), Svalbard, C) lower Khumbu glacier, Nepal (color figure available in online version).

Figure 2: Examples of imagery used for SfM model generation including 1896 terrestrial imagery from the Rhone glacier, high-oblique aerial photographs done during the 1936 Svalbard survey and handheld mixed images from 1978 over the lower Khumbu glacier.
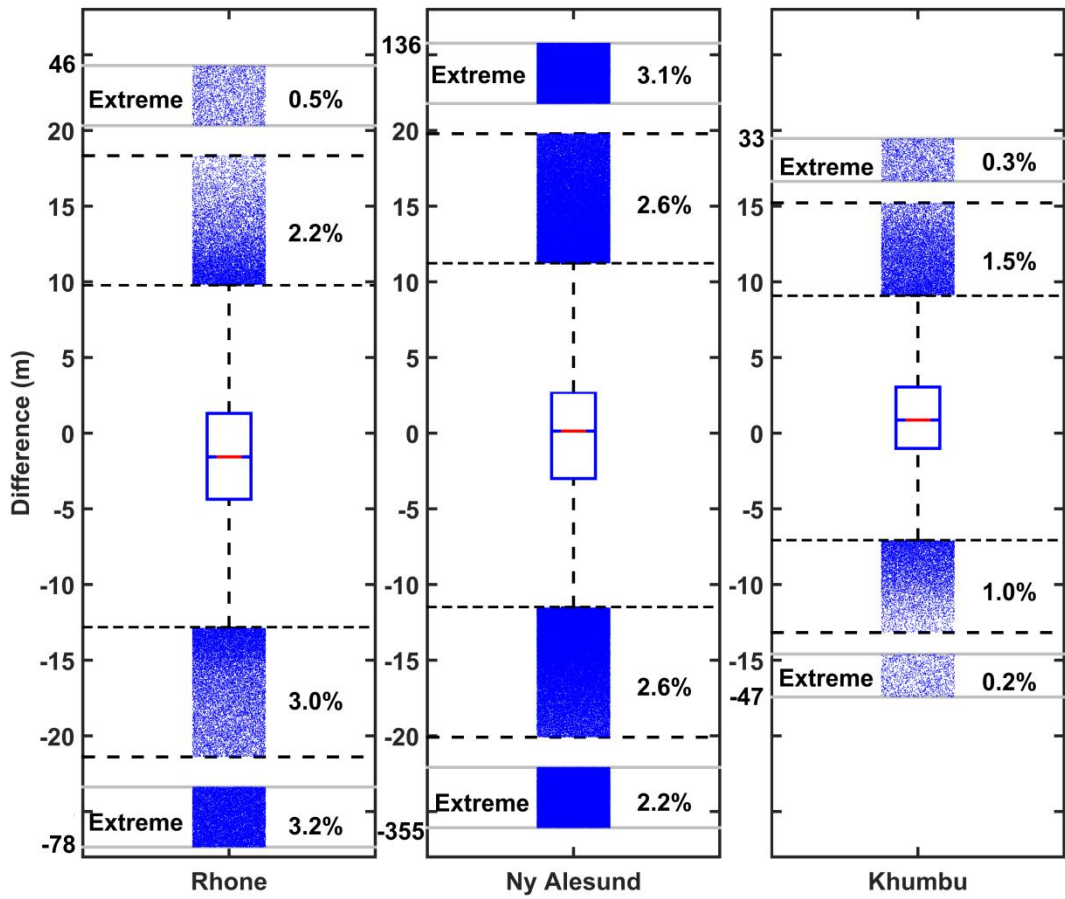
Figure 3: Box and whisker plots of the off glacier elevation differences showing the percentage of data considered extreme outliers and normal outliers, with the inner box upper and lower bounds being the limits the 25-75% of data. The center line represents the data median.
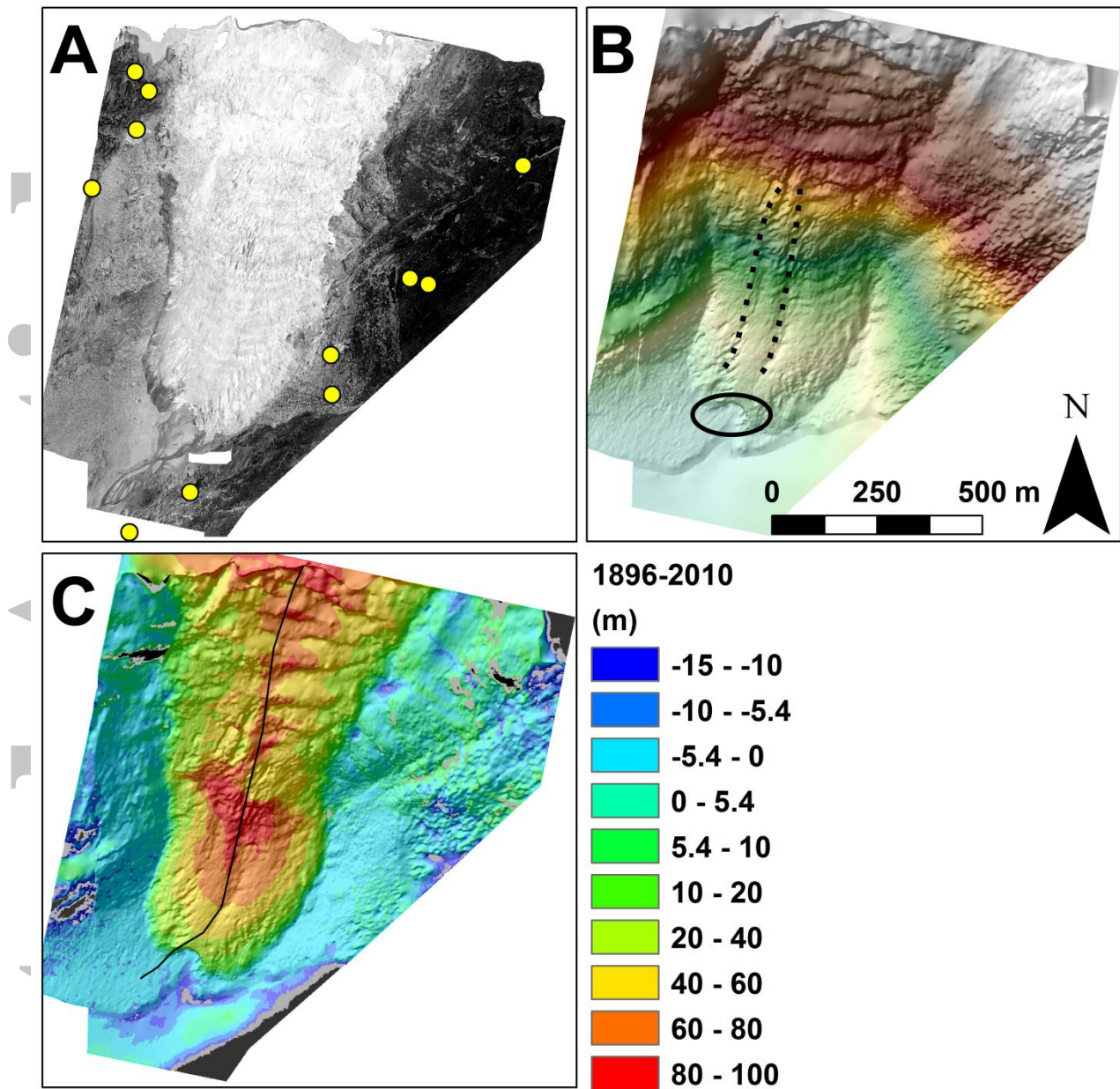
Figure 4: (A) Rhone glacier orthoimage, (B) 1896 DEM and (C) 1896-2010 elevation difference. Dotted lines indicate areas of surface depressions (B) and black oval shows outlet of subglacial meltwater in 1896 (B). Yellow dots mark locations of GCPs (A). Elevation profile of Figure 7 taken along solid black line (C) (color figure available in online version).
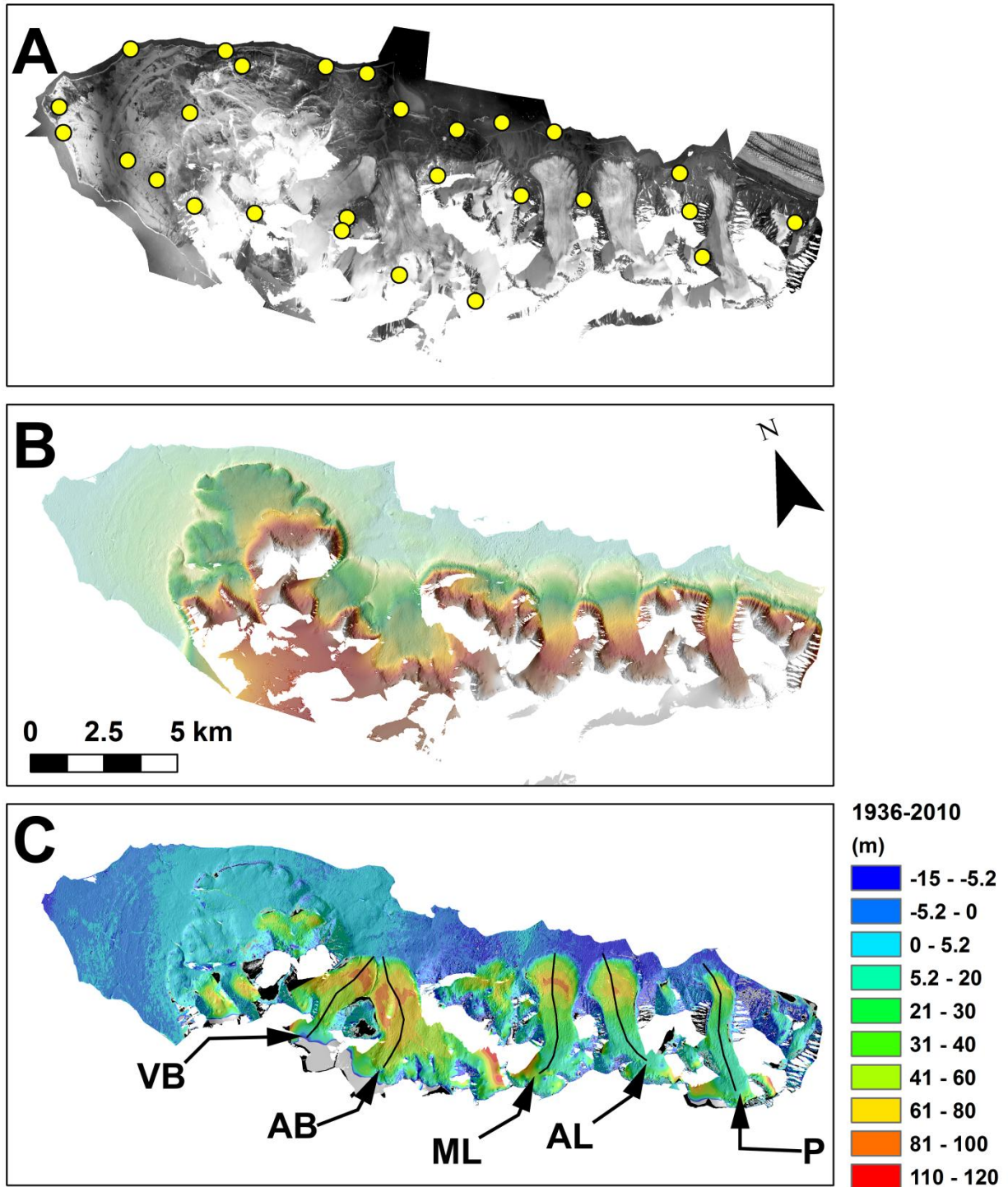
Figure 5: (A) Ny Ålesund orthoimage, (B) 1936 DEM and (C) 1936-2010 elevation difference. Yellow dots mark locations of GCPs (A). Elevation profiles of Figure 7 taken along solid black lines with individual glaciers marked Vestre Brøggerbreen (VB), Austre Brøggerbreen (AB), Midtre Lovénbreen (ML), Austre Lovénbreen (AL) and Pedersenbreen (P), in subset (C), (color figure available in online version).
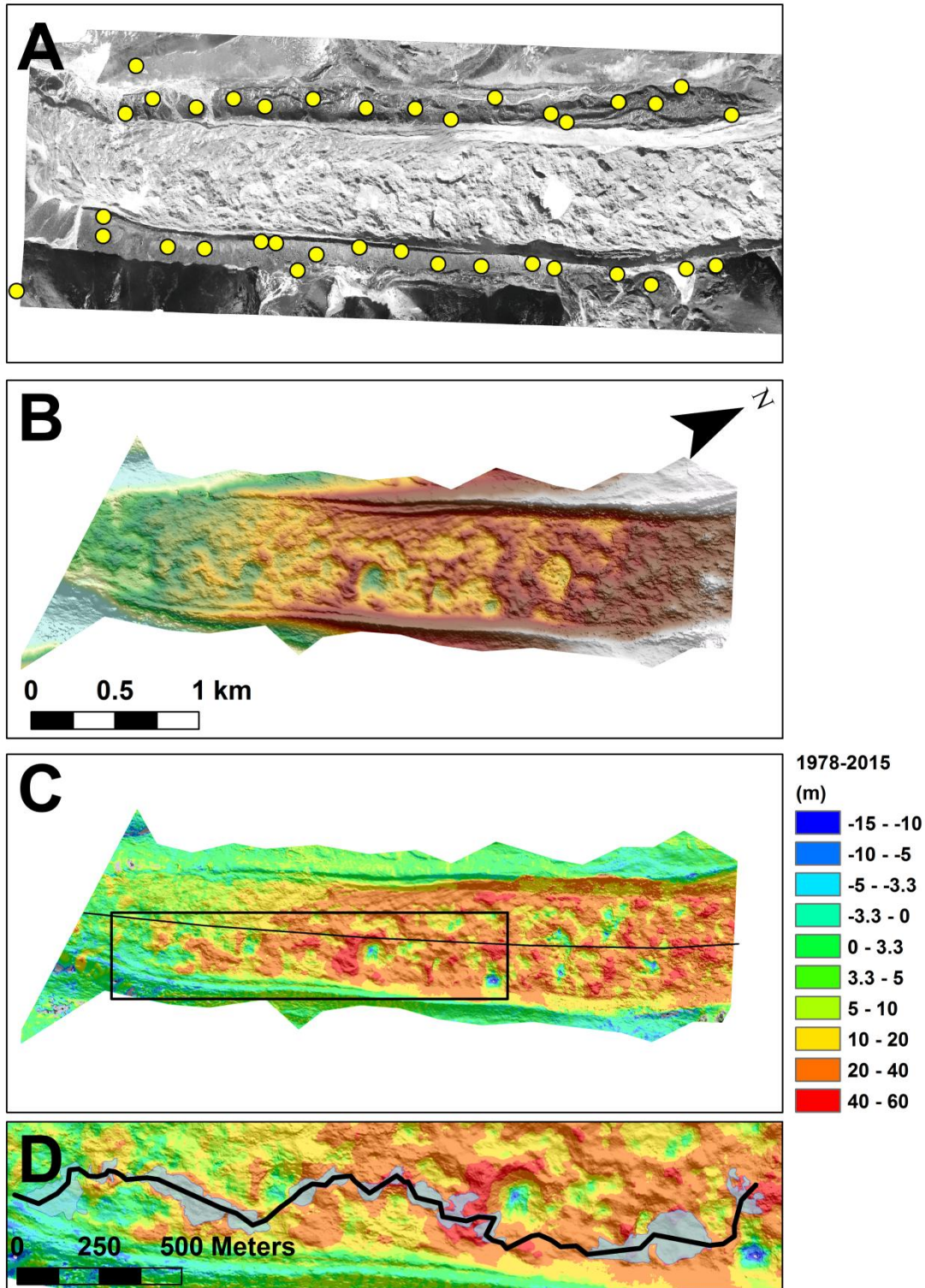
Figure 6: (A) Khumbu glacier orthoimage, (B) 1978 DEM, (C) 1978-2015 elevation difference and (D) 2015 lake system with Figure 12 transect (black). Yellow dots mark locations of GCPs (A). Elevation profile of Figure 7 taken along solid black line (C) (color figure available in online version).
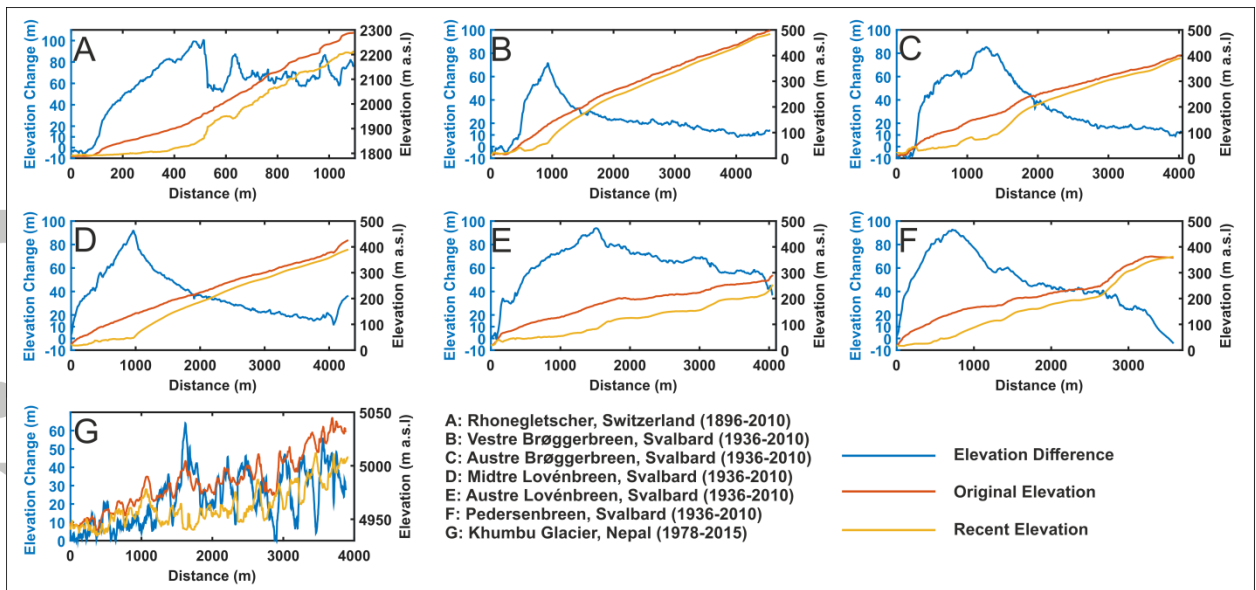
Figure 7: Elevation profiles from transects marked in Figures 4, 5 and 6 (color figure available in online version).
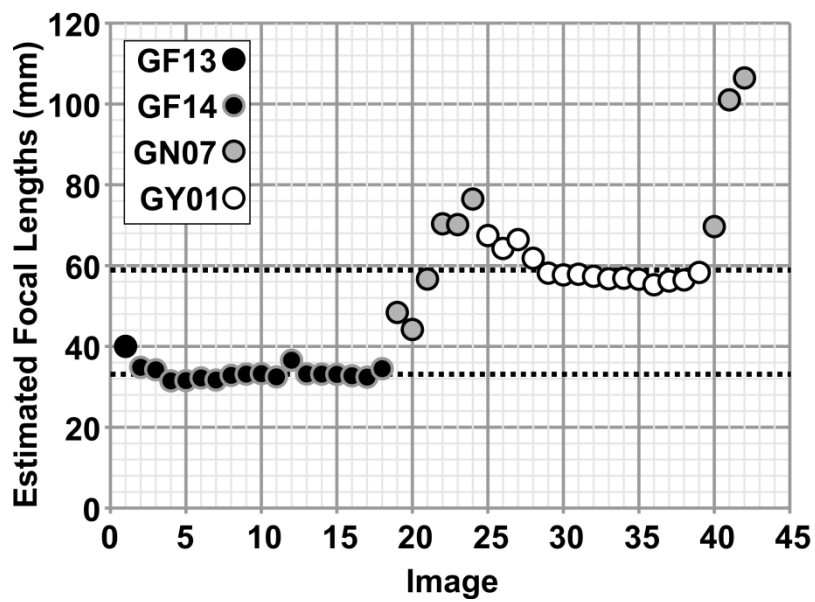
Figure 8: Scatter plot of estimated focal lengths of the images used for reconstruction of the Khumbu glacier. Note the two distinct focal lengths of ~33 mm and ~60 mm (GF14 and GY01) as well as imagery taken on one camera at multiple focal lengths (GN07).

Mean Estimated GSD 147mm (m/pix)
- 0.18 - 0.20
- 0.20 - 0.25
- 0.25 - 0.30
- 0.30 - 0.35
- 0.35 - 0.40
- 0.40 - 0.45
- 0.40 - 0.50
- 0.50 - 0.52

Mean Estimated GSD 210mm (m/pix)
- 1.32 - 1.50
- 1.50 - 1.75
- 1.75 - 2.00
- 2.00 - 2.25
- 2.25 - 2.50
- 2.50 - 2.75
- 2.75 - 2.87

Mean Estimated GSD (m/pix)
- 0.36 - 0.48
- 0.49 - 0.53
- 0.54 - 0.58
- 0.59 - 0.64
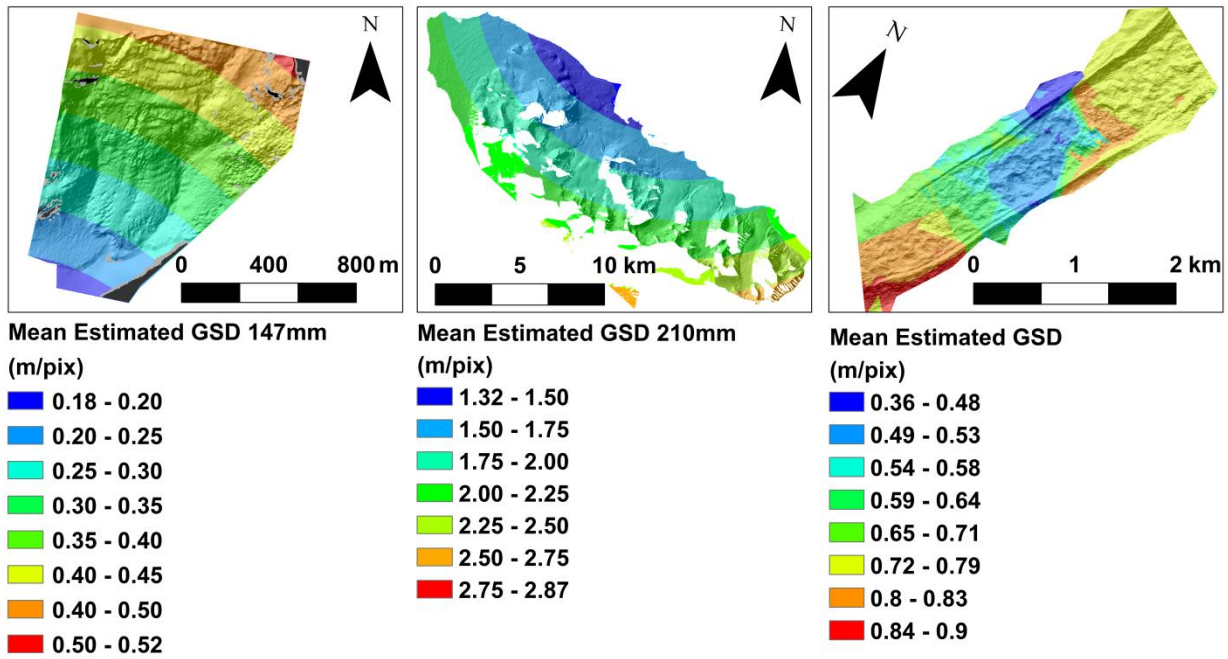- 0.65 - 0.71
- 0.72 - 0.79
- 0.8 - 0.83
- 0.84 - 0.9

Figure 9: Estimated GSD for all sites calculated with estimated IO and EO information from Photoscan (color figure available in online version).

Figure 10: Virtual view of the lower Rhone glacier as it was in 1896. The concave wall in the center of the terminus is the outlet of the englacial/subglacial meltwater.
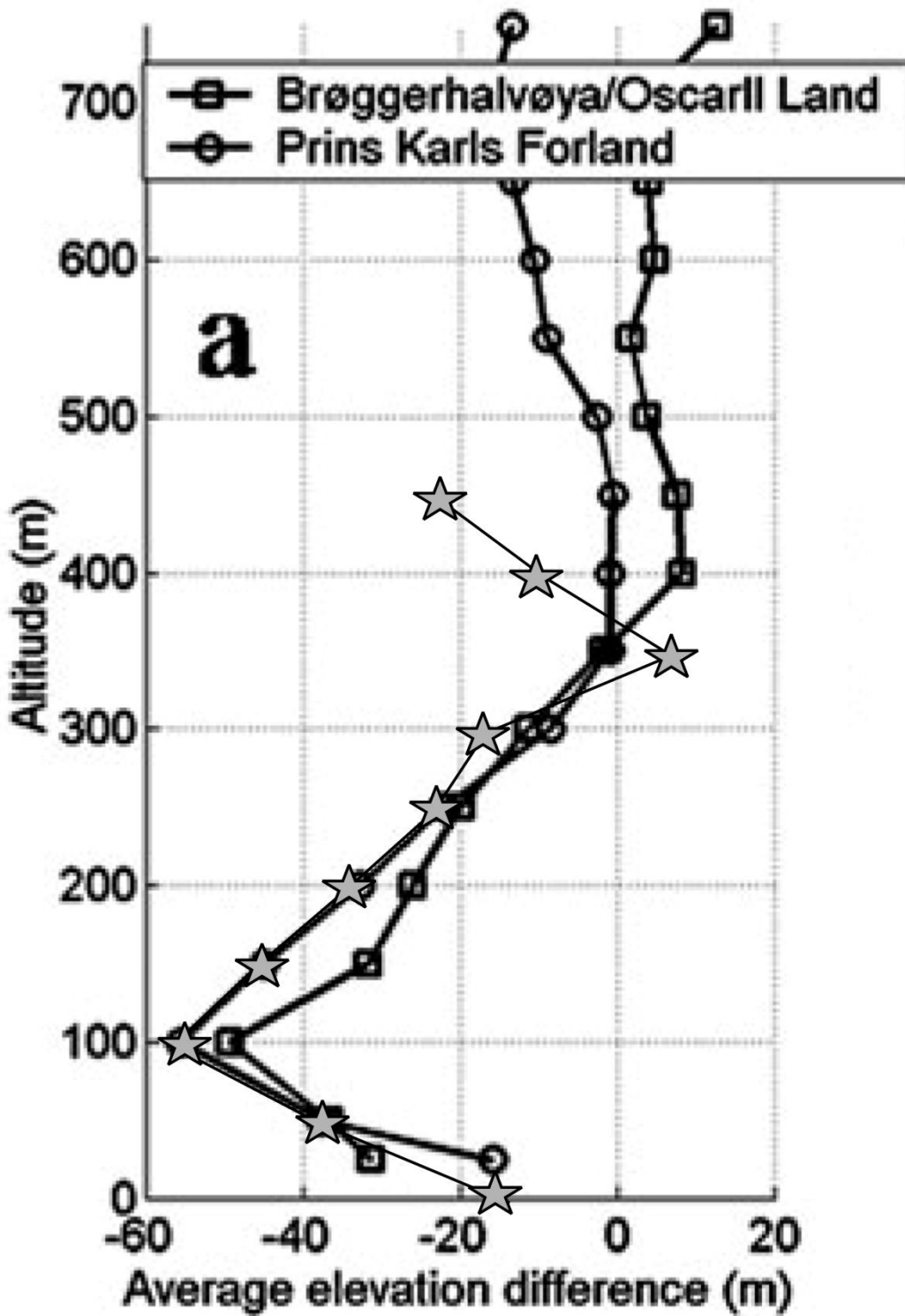
Figure 11: Mean elevation changes of 5 Ny Ålesund glaciers compared to results from Nuth et. al. (2007) comprised of all glaciers in the Brøggerhalvøya/Oscar II Land and Prins Karls Forland areas. Data from this study are plotted with gray stars and show very similar results with other glaciers in this region. Adapted from figure in Nuth et al. (2007).
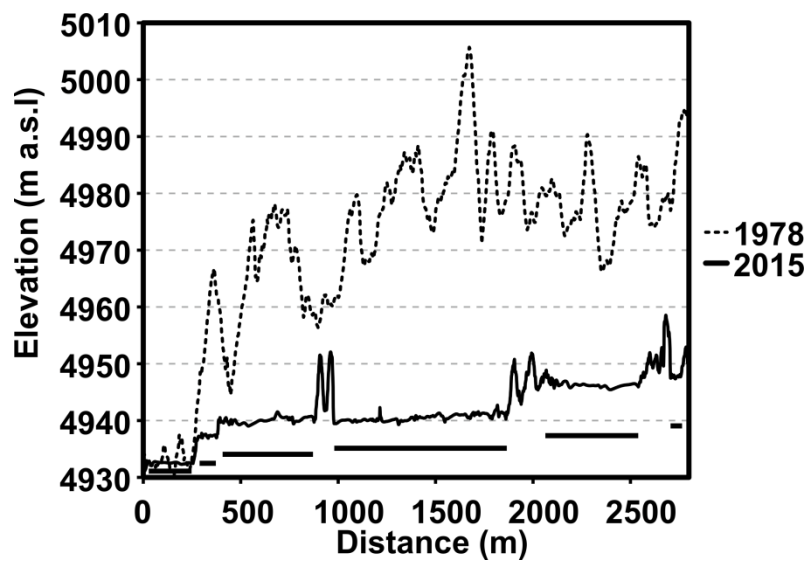
Figure 12: Elevation profile from lake system transect of the Khumbu glacier. Solid black horizontal bars indicate the locations of lake bodies in 2015.

Table 1: Photoscan processing settings used during model generation and orthomosaic creation.

	Rhone (1896)	Ny Alesund (1936)	Khumbu (1978)
General			
Cameras (#)	3	25	42
Markers (#)	14	27	32
GCP error (m)	2	5	5
Camera error (m)	2	5	5
Sparse Point Cloud			
Points	10,370	33,657	5,610
Gradual Selection Removal	reprojection error >1 pix, image count 2	reprojection error >1 pix, image count 2	reprojection error >1 pix, image count 2
Alignment Accuracy	Highest	High	Medium
Pair Preselection	Disabled	Disabled	Disabled
Dense Point Cloud			
Points	1,418,606	20,053,599	12,563,679
Reconstruction Parameters			
Quality	High	High	High
Depth filtering	Aggressive	Moderate	Moderate
Model			
Faces	180,000	12,036,707	
Vertices	90,642	6,020,370	
Reconstruction Parameters			
Surface Type	Arbitrary	Height field	
Source Data	Dense	Dense	
Interpolation	Enabled	Disabled	
Quality	Medium	High	
DEM			
Size (pix)	1216x1533	26680x19001	3578x4773
Source	Mesh	Mesh	Dense
Resolution (m)	1	2.3	1.4
Format	tiff	tiff	tiff
Orthoimage			
Blending Mode	Mosaic	Mosaic	Mosaic
Resolution (m)	0.2	1	0.5
Format	tiff	tiff	tiff

Table 2: Details of the resulting DEM and orthoimages generated through a SfM process for the three study locations.

	Rhone	Ny Ålesund	Khumbu
DEM Resolution (m)	1	2.3	1.46
Ortho Resolution (m)	0.2	1	1.3
Photoscan GCP 3D RMSE	7.24	13.4	5.15
Photoscan GCP Z RMSE	3.11	4.4	2.24
ΔZ RMSE (m)	1.45	0.24	0.001
ΔZ σ (including extreme outliers) (±m)	9.5	18.1	3.8
ΔZ σ (excluding extreme outliers) (±m)	5.4	5.2	2.8

Table 3: Off glacier elevation differences and distributions used to classify outliers and determine standard deviation of final DEMs. These data are shown in Figure 3.

	Off Glacier Differences (m)				Count (#)			Percent of Total		
	Rhone	Ny Alesund	Khumbu		Rhone	Ny Alesund	Khumbu	Rhone	Ny Alesund	Khumbu
Max	46.4	136.2	28.8	Upper Extreme Outliers	3114	93309	5246	0.5	3.1	1.1
Upper Extreme Outlier Limit	18.3	19.8	12.0	Upper Outliers	13983	78196	10469	2.2	2.6	2.3
Upper Outlier Limit	9.8	11.2	7.0	Upper Adjacent	141664	582281	99083	22.3	19.3	21.6
Q3	1.3	2.7	2.0		0	0	0	0.0	0.0	0.0
Q2/Median	-1.6	0.1	0.0	IQR	317532	1507580	229653	50.0	50.0	50.0
Q1	-4.4	-3.0	-1.4		0	0	0	0.0	0.0	0.0
Lower Outlier Limit	-12.9	-11.5	-6.4	Lower Adjacent	119377	609200	107364	18.8	20.2	23.4
Lower Extreme Outlier Limit	-21.4	-20.1	-11.4	Lower Outliers	18764	77832	3832	3.0	2.6	0.8
Min	-78.1	-355.3	-47.5	Lower Extreme Outliers	20617	66756	3610	3.2	2.2	0.8
				Total	635051	3015154	459257	100.0	100.0	100.0

Using Structure from Motion to create Glacier DEMs and Orthoimagery from Historical Terrestrial and Oblique Aerial Imagery

Jordan R. Mertes*, Jason D. Gulley, Douglas I Benn, Sarah S. Thompson, Lindsey I. Nicholson

Using historical glacier images, including terrestrial, professional high-oblique aerial and opportunistic aerial, we have successfully extracted high-quality DEMs and orthoimagery using the Structure from Motion method. In lieu of a priori camera information we demonstrated ground control data can be extracted from more recent datasets allowing us to georeference the models and to quantify longer-term glacial changes through DEM differencing. Using this method, we have unlocked the past and extracted valuable data, filling in gaps in the glacial observational records.